



ChemComm

**The core-shell engineering on energy product of magnetic nanometals**

|               |                          |
|---------------|--------------------------|
| Journal:      | <i>ChemComm</i>          |
| Manuscript ID | CC-COM-07-2018-005978.R1 |
| Article Type: | Communication            |
|               |                          |

SCHOLARONE™  
Manuscripts



Journal Name

COMMUNICATION

## The core-shell engineering on energy product of magnetic nanometals

Received 00th January 20xx,  
Accepted 00th January 20xx

Wei Zhang,<sup>a</sup> Weibing Yang,<sup>b</sup> Ravini U. Chandrasena,<sup>b</sup> V. Burak Özdöl,<sup>c</sup> Jim Ciston,<sup>c</sup> Michael Kornecki,<sup>d</sup> SelvaVennila Raju,<sup>d</sup> Raymond Brennan,<sup>d</sup> Alexander X. Gray,<sup>b</sup> and Shenqiang Ren\*

DOI: 10.1039/x0xx00000x

www.rsc.org/

**A solution-based growth of magnetic FePt-FeCo (core-shell) nanoparticles with controllable shell thickness is demonstrated. The transition from spin canting to exchange coupling of FePt-FeCo core-shell nanostructures leads to a 28% increase in the coercivity (12.8 KOe) and two-fold enhancement in the energy product (9.11 MGOe).**

Over the past few decades, magnetic nanoparticles have made significant contributions to modern technology, gaining interest for use in data storage materials, magnetic resonance imaging devices, and power generation systems.<sup>1</sup> However, with the growing concern over energy efficiency and environmental impact, earth-abundant magnetic materials with enhanced energy products are urgently needed. The rational design and growth of magnetic nanocomposites comprised of two or more materials has been considered a promising strategy to enhance the energy product of magnets.<sup>2-9</sup> In this context, magnetic core-shell nanocomposites that couple magnetically hard and soft phases could simultaneously achieve high magnetocrystalline anisotropy and saturation magnetization.<sup>6-10</sup> These core-shell architectures could efficiently tune magnetic properties (such as the thermal stability of magnetization and coercivity) via the control of core-shell parameters, including the shape, size, and chemical composition.<sup>13-16</sup> It has been shown that magnetic CoFe<sub>2</sub>O<sub>4</sub>-MnFe<sub>2</sub>O<sub>4</sub> core-shell nanoparticles with the interfacial spin interactions can be beyond the theoretical limit of their energy product.<sup>17</sup> There is an immediate need for simple,

scalable and reliable synthesis methods for manufacturing high-performance metallic core-shell nanocomposites with coupling interactions between the core and shell interfaces.

Here, a solution-based technique for the preparation of FePt-FeCo (core-shell) nanostructures with the controlled shell thickness is demonstrated. An interface coupling (spin canting) effect is evident in FePt-FeCo nanoparticles when the average thickness of the as-grown FeCo shell is 0.9±0.279 nm. Resulting core-shell FePt-FeCo nanoparticles indicate a substantial enhancement in magnetic coercivity (12.8 KOe), and a two-fold increase in the energy product (9.11 MGOe) at room temperature, compared to the FePt nanoparticles.

Figure 1a illustrates the schematic growth of FePt nanostructures with different morphologies. The FePt nanoparticles with average diameters of 2.8±0.183 nm was synthesized using dioctyl ether as the reaction solvent (Figure 1b). While switching the reaction solvent from dioctyl ether to oleyamine, the nanowire morphology is dominant in the as-synthesized FePt (Figure S1).<sup>18</sup> A variety of stoichiometric FePt nanoparticles with the chemical composition of Fe<sub>18</sub>Pt<sub>82</sub>, Fe<sub>42</sub>Pt<sub>58</sub>, and Fe<sub>61</sub>Pt<sub>39</sub> were synthesized by controlling the reaction conditions (Figure S2). It should be noted that the composition of as-synthesized Fe<sub>x</sub>Pt<sub>100-x</sub> had an influential effect on the size of resultant particles after sintering (Figure 1d).<sup>19</sup> By increasing the amount of Pt (Fe) during the sintering process, the extra Pt (Fe) atoms could be substitutionally placed on the L1<sub>0</sub> Fe (Pt) sublattice, effectively transforming the structure to a cubic phase with a reduced magnetocrystalline anisotropy.<sup>20</sup> Therefore, a lower phase transition temperature and increased particle growth could be demonstrated in either the sintered Pt-rich (Fe<sub>18</sub>Pt<sub>82</sub>; average particle size of 400 nm) or Fe-rich (Fe<sub>61</sub>Pt<sub>39</sub>; average particle size of 10 μm) particles,<sup>21</sup> while the stoichiometric Fe<sub>42</sub>Pt<sub>58</sub> nanoparticles could withstand higher sintering temperatures prior to the agglomeration, leading to a smaller particle size (the average diameter of 50 nm). The stoichiometry of FePt nanoparticles could also play a vital role in defining magnetic properties. As shown in Figure 1e, the as-synthesized Fe<sub>42</sub>Pt<sub>58</sub> nanoparticles exhibit a coercivity (H<sub>c</sub>) of 4500 Oe, a remanent

<sup>a</sup> Department of Mechanical and Aerospace Engineering, and Research and Education in Energy, Environment & Water (RENEW) Institute, University at Buffalo, The State University of New York, Buffalo, NY 14260.

<sup>b</sup> Department of Physics, Temple University, Philadelphia, Pennsylvania 19122, United States.

<sup>c</sup> National Center for Electron Microscopy Facility, Molecular Foundry, Lawrence Berkeley National Laboratory, Berkeley, California 94720, United States.

<sup>d</sup> U.S. Army Research Laboratory, Aberdeen Proving Ground, Maryland 21005, United States

\* Email: [shenren@buffalo.edu](mailto:shenren@buffalo.edu)

Electronic Supplementary Information (ESI) available: sample preparation and additional structural characterization. See DOI: 10.1039/x0xx00000x

magnetization ( $M_r$ ) of 17.5 emu/g, and a saturation magnetization ( $M_s$ ) of 27 emu/g. In contrast, the Fe-rich  $\text{Fe}_{61}\text{Pt}_{39}$  nanoparticles exhibit a larger saturation magnetization ( $M_s$ , 43 emu/g) and a much smaller coercivity ( $H_c$ , 510 Oe), while the Pt-rich  $\text{Fe}_{18}\text{Pt}_{82}$  nanoparticles demonstrate the lowest magnetic properties ( $M_s$  of 0.4 emu/g and  $H_c$  of 101 Oe). After sintering, the coercivity of  $\text{Fe}_{42}\text{Pt}_{58}$  nanoparticles could be increased to 10 KOe with a decrease in saturation magnetization (Figure 1f), suggesting a face-centered cubic (fcc) conversion to the  $\text{L1}_0$ -FePt structure confirmed by XRD.

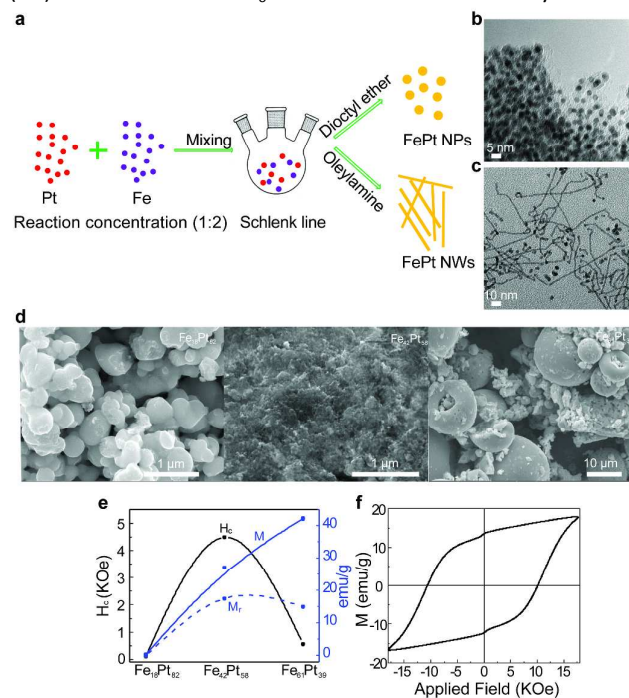


**Fig. 1. The solution growth of FePt nanostructures.** (a) Schematic process of FePt nanoparticle and nanowire growth, showing the importance of reaction solvents for morphological control. (b, c) Transmission electron microscopy (TEM) images of as-synthesized FePt nanoparticles and nanowires. (d) Scanning electron microscopy (SEM) images of FePt nanoparticles with different elemental ratios ( $\text{Fe}_{18}\text{Pt}_{82}$ ,  $\text{Fe}_{42}\text{Pt}_{58}$ , and  $\text{Fe}_{61}\text{Pt}_{39}$ ) after sintering at 773 K for 2 h. (e) Element ratio-dependent coercivity ( $H_c$ ), remanent magnetization ( $M_r$ ) and saturation magnetization ( $M_s$ ) of FePt nanoparticles after sintering at 773 K for 2 h. (f) The magnetic hysteresis loop of  $\text{Fe}_{42}\text{Pt}_{58}$  nanoparticles after sintering at 1023 K for 2 h at room temperature.

For magnetic alloys, strongly enhanced properties could be realized by coupling magnetically hard and soft phases that simultaneously achieve high magnetocrystalline anisotropy and high saturation magnetization. By varying the FeCo shell thickness, FePt-FeCo core-shell nanocrystals could be synthesized with properties close to their optimal values. For this reason, the as-synthesized FePt nanoparticles were mixed with Fe and Co precursors at 433 K, leading to the growth of FeCo shells. Figure 2a shows the schematic representation of the shell thickness control in FePt-FeCo core-shell nanoparticles. The average FeCo shell thickness was adjusted

from  $0.9 \pm 0.279$  nm to  $2.8 \pm 0.827$  nm at a constant stoichiometry of  $\text{Fe}_{42}\text{Pt}_{58}$  by increasing the precursor concentration (Figures 2a and S3). The details for the synthetic control were shown in the Supporting Information section. It should be noted that the reaction temperature was lower than the temperature of FeCo particle formation, as the pre-formed FePt cores served as nuclei from which the deposition of FeCo shells originated.

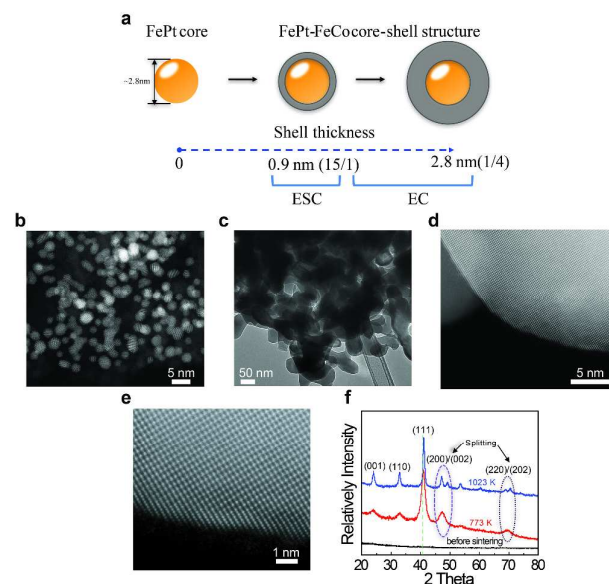


**Figure 2. The growth of FePt-FeCo core-shell nanoparticles.** (a) Schematic illustrations for synthesis of FePt-FeCo core-shell nanoparticles with tunable shell thickness (0.9 nm–2.8 nm). (b) TEM image of FePt-FeCo nanoparticles before sintering. (c) Low magnification TEM images of FePt-FeCo samples after sintering at 1023 K for 2 h. (d, e) High-resolution STEM images of annealed FePt-FeCo core-shell structures with the lattice ordering loss at the last  $\sim 1$  nm of surface shell. (f) XRD patterns of the as-synthesized FePt-FeCo before and after sintering at 773 K and 1023 K, respectively. The peak splitting indicates the phase transition from fcc to  $\text{L1}_0$  FePt.

Figure 2b shows a TEM image of the FePt-FeCo core-shell nanoparticles before sintering, with average shell thicknesses of  $0.9 \pm 0.279$  nm and homogeneous particle size distributions. The chemical compositions, containing constituent Fe, Pt and Co elements, were confirmed by energy dispersive X-ray spectroscopy (EDS, Figure S4). After sintering at 1023 K, the particles exhibited a heterogeneous distribution, with sizes ranging from 5 nm to 200 nm, as shown in Figures 2c–2e. High-resolution scanning TEM images of FePt-FeCo in Figure 2d provide the explicit microstructural details of the sample with the clear lattice fringes, confirming the high crystallinity of annealed FePt-FeCo. Furthermore, a  $\sim 1$  nm surface layer that lost the FePt  $\text{L1}_0$  ordering confirmed that an fcc-FeCo shell was formed (Figure 2e),<sup>22</sup> which was consistent with the XRD results (the standard ICDD data 00-026-1139, Figure 2f). The XRD spectra were further collected to investigate the effect of different sintering temperatures on phase evolution in the

FePt-FeCo structures (Figure 2f). Before sintering, no discernable diffraction peaks (black spectrum) were observed for the as-synthesized FePt-FeCo nanoparticles.<sup>23,24</sup> After sintering at 773 K (red spectrum), a series of diffraction peaks could be resolved, with the strong peaks corresponding to the (111) plane at 40.3° and the (200) plane at 47.2°, representing *fcc*-FePt nanostructures. After sintering at 1023 K (blue spectrum), the broad peaks became sharper, and more importantly, new shoulder peaks appeared at 49° and 71°, corresponding to the (002) and (202) planes, respectively. The splitting of peaks at 47.2° and 69.8° suggested phase transformation of FePt from *fcc* to *L1<sub>0</sub>*,<sup>25</sup> indicating the formation of *L1<sub>0</sub>* FePt at 1023K. In addition, the (111) peak shift (the green dash line in Figure 2f) was observed when compared with the standard ICDD data (00-026-1139), suggesting the existence of the FeCo shell. The related lattice distortion could be responsible for the enhanced energy product.

The correlation between the FeCo shell thickness and magnetic properties of FePt-FeCo was examined by measuring field-dependent magnetization. As shown in Figure 3a, the FePt-FeCo particles exhibited smooth magnetic hysteresis curves with insignificant variations, implying well-coupled core-shell phases. The FePt-only core had an  $H_c$  value of 10 kOe and a saturation magnetization ( $M_s$ ) of 17 emu/g (black dashed line). As the average thickness of the FeCo shell increased ( $2.1 \pm 0.148$  nm,  $2.4 \pm 0.436$  nm), the FePt-FeCo core-shell structures showed a corresponding increase in  $M_s$  from 88 to 104 emu/g.<sup>26</sup> In contrast, the  $H_c$  values exhibited a hyperbolic decrease when compared to the pure FePt sample. The thick ( $2.8 \pm 0.827$  nm) FeCo shell exhibited an  $H_c$  value of 487 Oe. The changes in  $H_c$  and  $M_s$  served as examples of exchange coupling (EC) behavior between magnetically hard FePt core and soft FeCo shells. However, as the shell thickness decreased ( $1.2 \pm 0.374$  nm,  $1.1 \pm 0.089$  nm,  $0.9 \pm 0.279$  nm), the FePt-FeCo nanoparticles exhibited an unusual phenomenon, with significantly increased  $H_c$  values to 8.2 kOe, 8.7 kOe, and 12.8 kOe, respectively. For the thin ( $0.9 \pm 0.279$  nm) FeCo shells, the  $H_c$  values of the FePt-FeCo nanostructures were 30% higher than that of FePt cores. Meanwhile, the decrease in  $M_s$  of FePt-FeCo nanostructures were relatively small, from 37 to 32 emu/g, but larger than that of the FePt cores. Figure 3b shows the relationship between  $M_s$  and  $H_c$  for FePt-FeCo nanostructures with different shell thicknesses. Unlike the typical core-shell nanoparticles in the EC regime (i.e. FePt-FeCo with a shell thickness larger than 2 nm), the thin-shelled FePt-FeCo nanoparticles possessed larger anisotropic energy barriers than the FePt core materials, which was representative of an enhanced spin canting effect (ESC) as opposed to exchange coupling.<sup>17, 27</sup> When the shell thickness was similar in size to the crystalline unit-cell (1 nm), the population of canted spins located at the interface between FePt cores and FeCo shells increased, requiring a larger external magnetic field to neutralize it. This was consistent with the enhanced  $H_c$  value,<sup>17, 27</sup> which could be attributed to the interfacial ESC effect.

The sintering temperature played an essential role in achieving phase transition of the magnetic FePt-FeCo nanostructures, leading to an investigation of these temperature effects on magnetic

properties of FePt-FeCo. As shown in Figure 3c, the FePt-FeCo nanoparticles with the shell thicknesses of  $0.9 \pm 0.279$  nm, exhibit a largely enhanced  $H_c$  values from 2.1 kOe to 12.8 kOe for the sintering temperature from 773 K to 1023 K, respectively. The relationship between  $M_s$  and  $H_c$  for FePt-FeCo ( $1.2 \pm 0.374$  nm,  $1.1 \pm 0.089$  nm,  $0.9 \pm 0.279$  nm) was plotted as a function of sintering temperature (Figure 3d). When compared to the change in  $M_s$ , a much larger increase in  $H_c$  was observed, indicating that the sintering temperature plays a significant role in the phase transition of FePt from *fcc* to *L1<sub>0</sub>*. Meanwhile, the slight decrease in  $M_s$  could be attributed to the diffusion of FeCo into the FePt core. The results indicated that the shell thickness played an important role in determining the magnetic properties of FePt-FeCo nanoparticles. The magnetic phenomenon in the ESC regime of as-prepared core-shell composites could potentially be utilized for the development of high-performance nanomagnets.

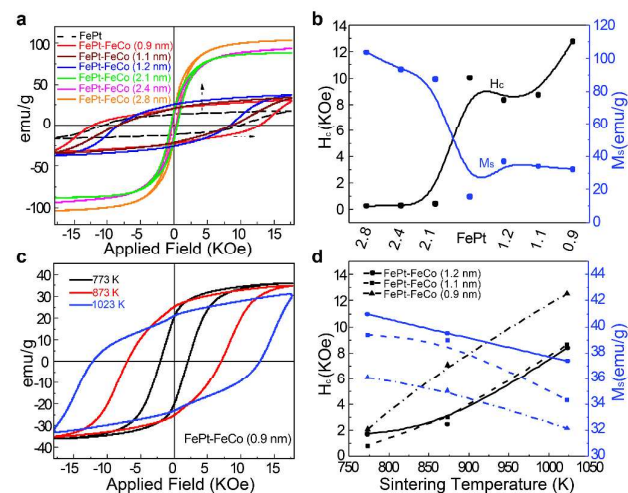


**Figure 3. Magnetic properties of FePt-FeCo core-shell nanoparticles.** (a) Magnetic hysteresis loops of FePt nanoparticles with various shell thicknesses measured at room temperature. (b) Shell thickness-dependent  $H_c$  and  $M_s$  curves of FePt-FeCo nanoparticles. (c) Sintering temperature-dependent magnetic hysteresis loops for FePt-FeCo nanoparticles with an average thickness of 0.9 nm. (d) Variation of  $H_c$  and  $M_s$  as a function of sintering temperature for FePt-FeCo with different shell thicknesses.

The controlled thickness of the FeCo shell onto the FePt core enabled tunability of the energy product ( $BH$ )<sub>max</sub> evolution in FePt-FeCo nanostructures. Figure 4a illustrates the B-H curves of sintered FePt cores, as well as a series of FePt-FeCo nanostructures with different shell thicknesses. As shown in Figure 4b, the measured ( $BH$ )<sub>max</sub> for the FePt core is 3.54 MGOe. The ( $BH$ )<sub>max</sub> value increased to 7.28 MGOe for the FePt-FeCo particles with  $0.9 \pm 0.279$  nm thick FeCo shells, indicating the effective ESC at the interface between the hard and soft phases. This energy product value decreased for thicker FeCo shells, but was much larger than that of pure FePt when the FeCo shell thickness was less than 1.2 nm (5.1 MGOe). This indicated that the energy product could be maximized such that the  $H_c$  could continue to grow and maintain a sufficiently high  $M_s$ . As the FeCo shell thickness was further increased, the  $M_s$  value



could not compensate for the drop in  $H_c$ , leading to a decrease in the  $(BH)_{\max}$  value. Therefore, the magnetic energy product performance was determined by the thickness of FeCo shell. Furthermore, the B-H curves of the samples with the thinnest shells ( $0.9 \pm 0.279$  nm) were also investigated at different sintering temperatures. The inset of Figure 4b displays the energy products of samples sintered at 773 K, 873 K, and 1023 K. The 873 K sintered sample exhibited an optimum energy product of 9.11 MGOe. This was attributed to FeCo shell diffusion at a higher sintering temperature of 1023 K, which led to saturation magnetization loss and minor separation between the two magnetic phases.

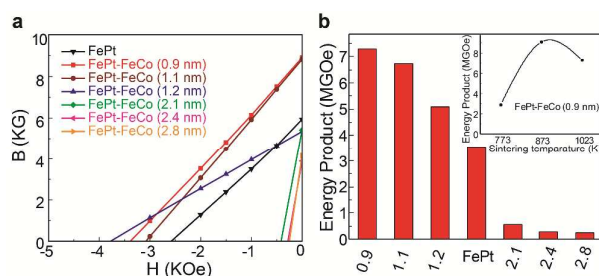


**Figure 4. Energy product of FePt-FeCo nanoparticles.** (a) Second-quadrant B-H curves for FePt-FeCo nanoparticles annealed at 1023 K for 2 h with different shell thicknesses. (b) Calculated energy products of samples shown in Figure 4a, with the inset showing the calculated energy products for FePt-FeCo with shell thicknesses of 0.9 nm after sintering at different temperatures for 2h.

Ultimately, a solution-based nano-synthesis method was developed by coating a magnetically soft FeCo shell onto a hard FePt core to produce core-shell nanostructures with controlled shell thickness. The exchange coupling and enhanced spin canting effects were realized by controlling the FeCo shell thickness, leading to enhanced coercivities and increased energy products in FePt-FeCo nanostructures. The spin canting techniques provided new opportunities for designing high performance magnetic core-shell nanostructures.

## Conflicts of interest

There are no conflicts to declare.

## Acknowledgements

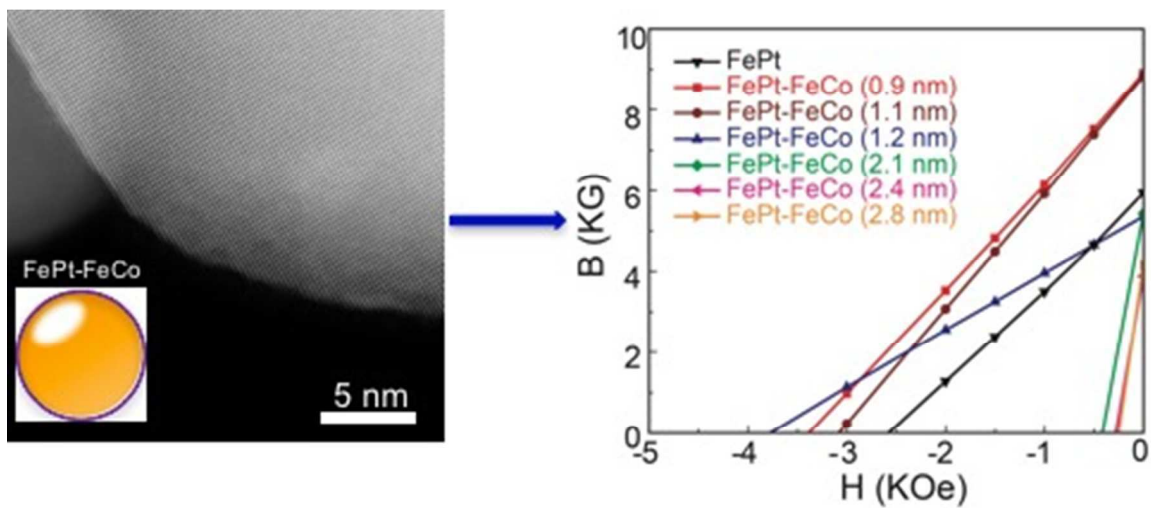
S.R. acknowledges the support from the U.S. National Science Foundation (NSF) under the CAREER Award No: NSF-DMR-1830749. A.X.G. acknowledges support from the U.S. Army Research Office, under Grant No. W911NF-15-1-0181. Work at the Molecular Foundry was supported by the Office of Science, Office of Basic Energy Sciences, of the U.S. Department of Energy under Contract No. DE-AC02-05CH11231. Research reported in this document was supported in part by contract W911-QX-16-D-0014 under SURVICE Engineering and W911NF-16-2-0050 under Oak Ridge Institute for Science and Education through an interagency agreement between the U.S. Department of Energy and the U.S. Army Research Laboratory. The views and conclusions contained in this document are those of the authors and should not be interpreted as representing the official policies, either expressed or implied, of the Army Research Laboratory or the

U.S. Government. The U.S. Government is authorized to reproduce and distribute reprints for Government purposes not withstanding any copyright notation herein.

## Notes and references

- Lu, A. H.; Salabas, E. e. L.; Schüth, F. *Angewandte Chemie International Edition* 2007, **46**(8), 1222-1244.
- Liu, X.; He, S.; Qiu, J.-M.; Wang, J.-P. *Applied Physics Letters* 2011, **98**(22), 222507.
- De Sousa, N.; Apolinario, A.; Vernay, F.; Monteiro, P.; Albertini, F.; Casoli, F.; Kachkachi, H.; Schmool, D. *Physical Review B* 2010, **82**(10), 104433.
- Kawald, U.; Zemke, W.; Bach, H.; Pelzl, J.; Saunders, G. *Physica B: Condensed Matter* 1990, **161**(1-3), 72-74.
- Carnevale, D. J.; Shatruk, M.; Strouse, G. F. *Chemistry of Materials* 2016, **28**(15), 5480-5487.
- Lee, J.H.; Jang, J.T.; Choi, J.S.; Moon, S.H.; Noh, S.H.; Kim, J.W.; Kim, J.G.; Kim, I.S.; Park, K.I.; Cheon, J. *Nature nanotechnology* 2011, **6**(7), 418.
- Liu, F.; Zhu, J.; Yang, W.; Dong, Y.; Hou, Y.; Zhang, C.; Yin, H.; Sun, S. *Angewandte Chemie* 2014, **126**(8), 2208-2212.
- Carnevale, D.J.; Shatruk, M.; Strouse, G.F. *Chemistry of Materials* 2016, **28**(15), 5480-5487.
- Yang, C.; Jia, L.; Wang, S.; Gao, C.; Shi, D.; Hou, Y.; Gao, S. S. *Scientific reports* 2013, **3**, 3542.
- Kneller, E. F.; Hawig, R. *IEEE Transactions on Magnetics* 1991, **27**(4), 3588-3560.
- Liu, F.; Hou, Y.; Gao, S. *Chemical Society Reviews* 2014, **43**(23), 8098-8113.
- Song, Q.; Zhang, Z. J. *Journal of the American Chemical Society* 2012, **134**(24), 10182-10190.
- Zeng, H.; Li, J.; Liu, J. P.; Wang, Z. L.; Sun, S. *Nature* 2002, **420**(6914), 395-398.
- Zhang, W.; Patel, K.; Ren, S. *Nanoscale* 2017, **9**(35), 13203-13208.
- Xu, C.; Xu, K.; Gu, H.; Zheng, R.; Liu, H.; Zhang, X.; Guo, Z.; Xu, B. *Journal of the American Chemical Society* 2004, **126**(32), 9938-9939.
- Gao, J.; Gu, H.; Xu, B. *Accounts of chemical research* 2009, **42**(8), 1097-1107.
- Moon, S. H.; Noh, S.-h.; Lee, J.-H.; Shin, T.-H.; Lim, Y.; Cheon, J. *Nano Letters* 2017, **17**(2), 800-804.
- Wang, C., Hou, Y., Kim, J. and Sun, S. *Angewandte Chemie* 2007, **119**(33), 6449-6451.
- Chen, W.; Kim, J.; Sun, S.; Chen, S. *Langmuir* 2007, **23**(22), 11303-11310.
- Klemmer, T.; Shukla, N.; Liu, C.; Wu, X.; Svedberg, E.; Mryasov, O.; Chantrell, R.; Weller, D.; Tanase, M.; Laughlin, D. *Applied Physics Letters* 2002, **81**(12), 2220-2222.
- Müller, M.; Albe, K. *Physical Review B* 2005, **72**, (9), 094203.
- Kim, J.; Rong, C.; Liu, J. P.; Sun, S. *Advanced Materials* 2009, **21**(8), 906-909.
- Chen, B.; Lutker, K.; Raju, S. V.; Yan, J.; Kanitpanyacharoen, W.; Lei, J.; Yang, S.; Wenk, H.-R.; Mao, H.-k.; Williams, Q. *Science* 2012, **338**(6113), 1448-1451.
- Petkov, V.; Shastri, S. D. *Physical Review B* 2010, **81**(16), 165428.
- Medwal, R.; Sehdev, N.; Annapoorni, S. *Journal of Physics D: Applied Physics* 2012, **45**(5), 055001.
- Gutfleisch, O.; Lyubina, J.; Müller, K. H.; Schultz, L. *Advanced Engineering Materials* 2005, **7**(4), 208-212.
- Tanaka, T.; Matsuzaki, J.; Kurisu, H.; Yamamoto, S. *Journal of Magnetism and Magnetic Materials* 2008, **320**(22), 3100-3103.

## TOC



Spin canting effect in FePt-FeCo (core-shell) nanostructures enhances magnetic energy product.